



Response of Electric Field in Terrestrial Magnetosphere to Interplanetary Shock

Dianjun Zhang^{1,2} , Wenlong Liu^{1,2} , Junfeng Du^{1,2}, Yiqun Yu^{1,2} , Xinlin Li³ , Theodore E Sarris^{3,4} , and Jinbin Cao^{1,2} ¹ School of Space and Environment, Beihang University, Beijing, People's Republic of China; liuwenlong@buaa.edu.cn² Key Laboratory of Space Environment Monitoring and Information Processing of MIT, Beihang University, Beijing People's Republic of China³ Laboratory for Atmospheric and Space Physics, University of Colorado Boulder, Boulder, CO, USA⁴ Department of Electrical and Computer Engineering, Democritus University of Thrace, Xanthi, Greece

Received 2022 March 30; revised 2022 July 15; accepted 2022 September 7; published 2022 October 14

Abstract

Electric field impulses generated by interplanetary shocks can cause a series of dynamic processes in the Earth's magnetosphere and were previously explained by either fast-mode wave propagation or flow related to compression of the magnetopause. Based on a Space Weather Modeling Framework simulation, we suggest a new scenario in which the evolution of the impulse is due to both the propagation of the fast-mode wave and the compression of the magnetopause, which can explain the simulation and observations in previous related studies. The onset of the electric field impulse is determined by the propagation of the fast-mode wave in the magnetosphere while the peak of the impulse is determined by the propagation of the compression of the magnetopause. The new understanding of the impulse is important for the generation of subsequent ultralow frequency waves through the coupling of the fast-mode to Alfvén waves and field line resonances and related radiation-belt electron acceleration.

Unified Astronomy Thesaurus concepts: [Space plasmas \(1544\)](#); [Space weather \(2037\)](#); [Van Allen radiation belts \(1758\)](#); [Planetary magnetospheres \(997\)](#); [Magnetohydrodynamical simulations \(1966\)](#); [Magnetohydrodynamics \(1964\)](#); [Solar-terrestrial interactions \(1473\)](#); [Solar-planetary interactions \(1472\)](#); [Interplanetary shocks \(829\)](#)

Supporting material: animation

1. Introduction

Interplanetary shock (IPS)'s compression of the Earth's magnetosphere can cause various dynamic changes in the radiation belt, such as prompt injection and acceleration of relativistic electrons (with energies $E > 1.5$ MeV) (Blake et al. 1992; Foster et al. 2015; Kanekal et al. 2016; Schiller et al. 2016) and particle precipitation that may further cause an aurora (Li et al. 2016; Zhang et al. 2003; Zhou & Tsurutani 1999). The electric field impulses induced by IPS compression have been proven to be a direct driver of MeV electrons acceleration and transport in the Earth's radiation belt (Hudson et al. 2017, 2015; Kress et al. 2007; Li et al. 1993; Liu et al. 2019; Patel et al. 2019). Impacts of IPS on the magnetosphere may also generate ultralow frequency (ULF) waves through the field line resonance mechanism (Liu et al. 2009, 2010, 2013; Fu et al. 2011, 2012; Baumjohann et al. 1984; Eriksson et al. 2006; Hao et al. 2014, 2019; Hudson et al. 2004; Shi et al. 2014; Zhang et al. 2010), which may further resonate with drifting electrons (Hao et al. 2014, 2019; Korotova et al. 2018; Zong et al. 2009).

In response to the IPSs' compression, an impulsive enhancement of the magnetic field magnitude and the inductive dawnward electric field in the dayside magnetosphere are common features (Araki 1997; Wang et al. 2009). Based on the multispacecraft observation, the propagation speed of the compressional wave front of impulse has been calculated from the onset timing of magnetic or electric field variations (Cattell et al. 2017; Takahashi et al. 2017; Wilken et al. 1982; Zong et al. 2009). The calculated propagation velocities of the

impulses are on the order of the fast-mode (magnetosonic) speed, which is equal to local Alfvén speed (about $600\text{--}1000\text{ km s}^{-1}$) with cold plasma assumption in the inner magnetosphere, and is predominantly in the antisunward direction. It is thus suggested that the propagation of the electric field impulse is related to tailward-propagating fast-mode wave launched at magnetopause. However in recent studies (Kim et al. 2012; Korotova et al. 2018; Zhang et al. 2018), spacecraft measurements have found that the peaks of the electric field impulses are primarily in the azimuthally westward direction, in contradiction to the fast wave propagation scenario where the electric field is in the dawn–dusk direction throughout the magnetosphere.

On the other hand, some observation and simulation studies (Kim et al. 2009, 2012; Sun et al. 2015) suggest that the impulsive signature of the magnetospheric electric field is induced by the plasma motion associated with the compression on the magnetopause, which suggests that the propagation of the electric field impulse is related to the passage of an IPS. The plasma motion and the impulsive signatures further evolve into vortex-like structures in the magnetospheric flank (Shi et al. 2014). However, this scenario makes it difficult to explain the tailward-propagating speed calculated from multispacecraft onset timing, as the propagation speed of the IPS is generally slower than the fast-mode speed in the magnetosphere (Kim et al. 2009; Sibeck 1990). Therefore, neither scenario can completely explain the observations.

To further investigate the IPS compression on the Earth's magnetosphere, the Space Weather Modeling Framework (SWMF; Tóth et al. 2005) is used to simulate the interaction between IPS and the Earth's magnetosphere as described in 3 Section. SWMF integrates a global magnetohydrodynamic (MHD) simulation model and has been proven to be capable of investing the global fields and plasma dynamics in the



Original content from this work may be used under the terms of the [Creative Commons Attribution 4.0 licence](#). Any further distribution of this work must maintain attribution to the author(s) and the title of the work, journal citation and DOI.

magnetosphere (Yu & Ridley 2009, 2011). A new scenario that can explain previous observations is proposed based on the global picture of the evolution of impulsive electric fields presented by simulation results.

2. Observation

On 2015 March 17, an IPS was observed at $\sim 04:00$ UT by the Wind spacecraft located near the Lagrangian-1 point (L1) in the Sun–Earth system. Shortly after, $\sim 04:45$ UT, the IPS impacted the Earth’s magnetosphere, as indicated by the rise of the SYM-H geomagnetic index from 15 to 70 nT. The resulting geomagnetic storm, known as the St. Patrick’s Day 2015 event, is the most powerful geomagnetic storm of the previous solar cycle, reaching a minimum Disturbance Storm Time index (*Dst*) of -223 nT. Due to its scale, this event has been investigated extensively from many aspects, such as prompt injection and acceleration of energetic electrons (Kanekal et al. 2016; Hudson et al. 2017), fast radial diffusion driven by ULF waves (Jaynes et al. 2018; Ozeke et al. 2019), enhancement of plasmasphere and ring current dynamic (Goldstein et al. 2017), ionospheric disturbances induced by energy inputs into the high-latitude regions (Lyons et al. 2016; Prikryl et al. 2016; Marsal et al. 2017; De Michelis et al. 2020; Papadimitriou et al. 2020), significant subauroral processes related to magnetosphere–ionosphere coupling (Wei et al. 2019a; Zhang et al. 2017; Yue et al. 2016), and changes in global neutral wind driven by high-latitude energy and momentum inputs (Dmitriev et al. 2017; Zakharenkova et al. 2016).

In this paper, we focus on the generation, evolution, and propagation of the IPS-induced impulsive electric field during this storm sudden commencement, which is responsible for the prompt acceleration of energetic electrons. For this investigation, we used observational data obtained from multiple spacecraft and observatories. Data sources include thermal plasma measurements from the 3D Plasma and Energetic Particle Investigation (3DP) instrument (Lepping et al. 1995) on board the Wind spacecraft (Lepping et al. 1990); magnetic field data from the Electric and Magnetic Field Instrument Suite and Integrated Science (EMFISIS; Kletzing et al. 2013), and electric field data from the Electric Field and Waves (EFW) instrument (Wygant et al. 2013) on board the Van Allen Probes (Mauk et al. 2013). All observational data in this study can be accessed from NASA Space Physics Data Facility website.⁵

An overview of the event as measured by the Wind spacecraft in the solar wind and the Van Allen Probes in the magnetosphere is given in Figure 1. Figure 1(a) summarizes the observation on the IPS at L1 point in the 3 s resolution solar wind data measured by 3DP and the Magnetic Field Instrument (MFI) on board the Wind spacecraft showing the proton number density increasing from 10 to 30 cm^{-3} , the solar wind velocity increasing from 400 to 550 km s^{-1} , the proton temperature increasing from 5 to 20 K, and the interplanetary magnetic field (IMF) increasing from 10 to 30 nT. At $\sim 04:45$ UT, Van Allen Probe A (VAP-A) was located in the dusk sector at magnetic local time (MLT) ~ 20 and $L = 4.9$ while Van Allen Probe B (VAP-B) is located in the midnight sector at MLT ~ 2 and $L = 3.2$ as shown in Figure 1(b). Both probes observed variations in the magnetic and electric fields resulting from the IPS’s compression of the Earth’s magnetosphere as shown in the second and fourth panels of Figure 1(c), which

shows the magnetic field magnitude (B_{total}) and the y component of electric field (E_y) in the Geocentric Solar Ecliptic (GSE) coordinate system respectively. It is worth noting that the EFW instrument on VAP-A observed a single positive E_y impulse with an amplitude of 3.0 mV m^{-1} while VAP-B initially observed a relatively weaker negative E_y variation with an amplitude of -2.7 mV m^{-1} followed by a stronger positive impulse with an amplitude of 7.5 mV m^{-1} , showing as a dip prior to the impulse. The orientation of the shock-induced electric field impulse in the Van Allen Probes’ observation is consistent with observations and the statistical results of previous related studies (Araki 1997; Cattell et al. 2017; Shinbori et al. 2004; Takahashi et al. 2017; Zhang et al. 2018).

3. Methodology and Simulation

SWMF is used in this study to simulate the propagation characteristics of the electric field impulse induced by the IPS on the magnetosphere. The framework is equipped with a global MHD model BATS-R-US (Powell et al. 1999), a ring current model Rice Convection Model (Toffoletto et al. 2003), and an ionospheric electrodynamic solver (Ridley et al. 2004). The global MHD model solves the ideal MHD equations to represent the global magnetosphere driven by upstream solar wind conditions obtained from the Wind spacecraft measurements. The solar wind data are interpolated into a time axis with uniform time resolution of 5 s before being input to the simulation. The conditions were shifted to the upper boundary of the model at $32 R_E$ before driving the model. The model is designed with adaptive grid resolutions. For $r < 4 R_E$, a resolution of $1/8 R_E$ is used; for the outer region with $r < 12 R_E$, a coarser resolution of $1/4 R_E$ is applied. The Rice Convection Model (RCM) is used to determine the ring current plasma pressure in the inner magnetosphere, which is then passed to the global MHD model to compensate for the missing kinetic physics therein. The details of the two-way coupling between the two models can be found in De Zeeuw et al. (2004). The ionospheric electrodynamic solver determines electric potential using height-integrated conductance and the field aligned currents (FACs). The FAC is calculated at $3.5 R_E$ of the MHD model and mapped along field lines down to the ionospheric altitude (~ 110 km). The conductance is specified based on the solar irradiance and auroral precipitation, using empirical formulas in Ridley et al. (2004). The resultant electric potential is then passed to both the inner boundary of the global MHD model and the RCM, for setting up the inner boundary velocity and electric drift velocity, respectively. The SWMF is capable of solving and picturing the magnetospheric response to solar wind dynamic pressure enhancements (Yu & Ridley 2009, 2011; Samsonov et al. 2010) and has been widely validated (Wang et al. 2008; Yu & Ridley 2008; Welling & Ridley 2010; Rastätter et al. 2013). Previous studies also have reproduced the magnetosphere–ionosphere coupling process during the same St. Patrick’s Day magnetic storm with SWMF’s simulation (Wei et al. 2019a, 2019b; Kubyskhina et al. 2019).

The 2015 March 17 event has been widely reported in several published studies on the transport and acceleration of energetic electrons (Hudson et al. 2017; Kanekal et al. 2016). In this study, in order to explain the observations and reveal the evolution and the propagation characteristics of the electric field impulse, we performed a SWMF simulation with high

⁵ <https://cdaweb.gsfc.nasa.gov>

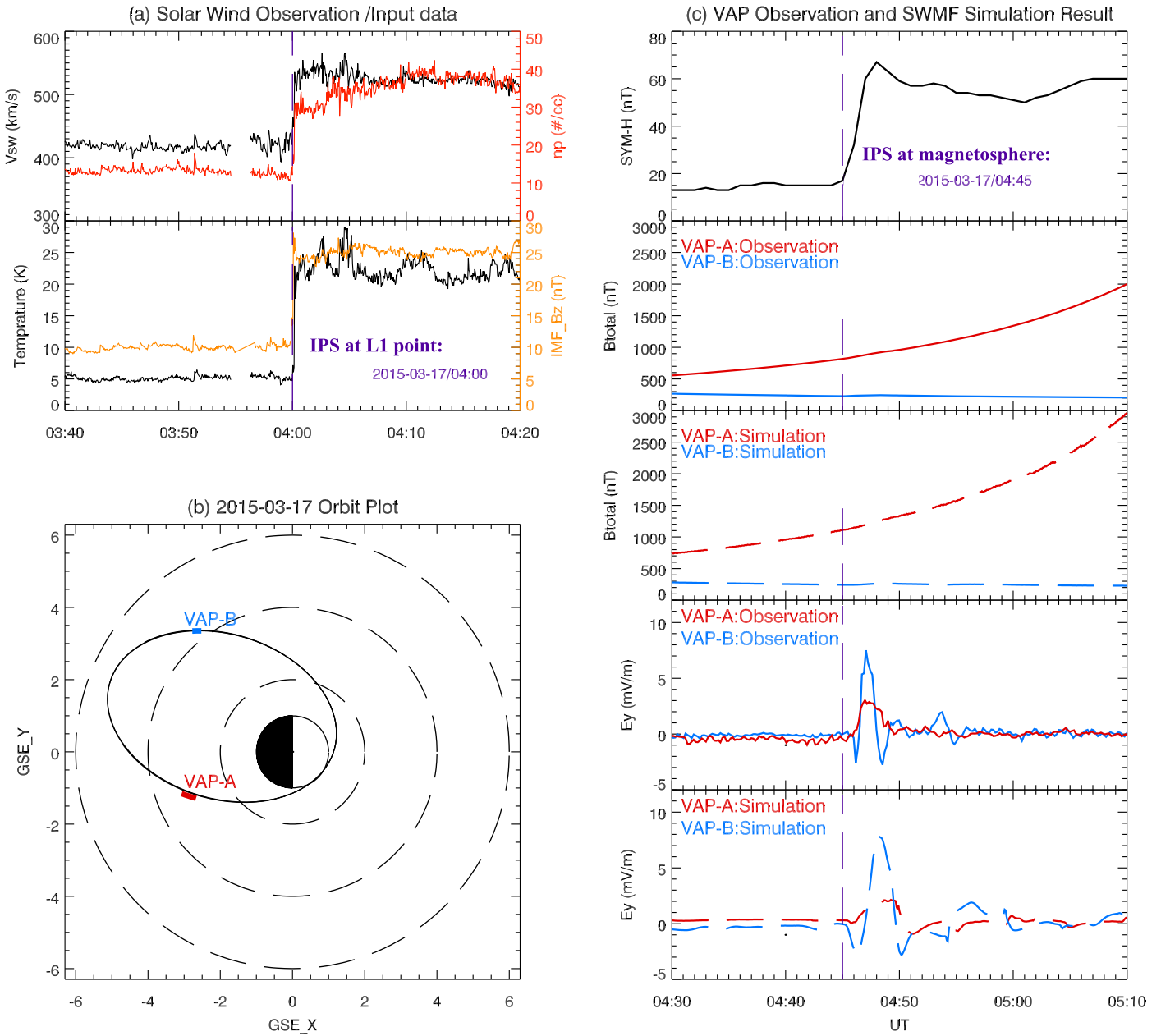


Figure 1. Overview of the IPS event on 2015 March 17. (a) Solar wind measurements by Wind spacecraft. (b) Orbital information of Van Allen Probes spacecraft. (c) Van Allen Probes observations and SWMF simulation results. From top to bottom, geomagnetic index SYM-H, observed magnetic field magnitude, simulated magnetic field magnitude, observed electric field y component, and simulated electric field y component are plotted.

time resolution of 5 s and with the input of the solar wind data shown in Figure 1(a), as described in detail in the 2 Section. The simulated B_{total} and E_y at the location of Van Allen Probes (shown in Figure 1(b)) are shown in the third and fifth panels of Figure 1(c). The main features of the electric field observed by the two spacecraft, including the timing and amplitude, are well reproduced in the simulations suggesting the credibility of the simulation results.

Figure 2 presents the evolution of the equatorial electric field vector, equatorial flow vector, and the magnetic field magnitude obtained from the simulation for five time frames, as marked. The location of IPS front at each time frame is indicated by a blue arrow above each panel. An animation of this simulation can be found with Figure 2. From Figures 2(a) to (e), it can be seen that the direction of electric field impulse

turns from dawnward on dayside to duskward on nightside. The direction of the electric field impulses with the largest amplitudes are generally in the westward azimuthal direction especially in the range of $L < 6.6$. These signatures are consistent with previous observations suggesting that the impulses are generated by a global compression of the magnetosphere (Korotova et al. 2018; Shinbori et al. 2004; Zhang et al. 2018). Note that in Figure 2(e) electric field turns duskward at 4:49 UT on the dayside, which is possibly due to the drop that is seen in the IMF B_z right after the passage of the pressure pulse as shown in Figure 1(a) producing a curl of the electric field with an opposite sign.

Besides the dawn–dusk component of electric field (E_y), the azimuthal component of electric field (E_a) is also investigated in this study since this component is westward and antiparallel

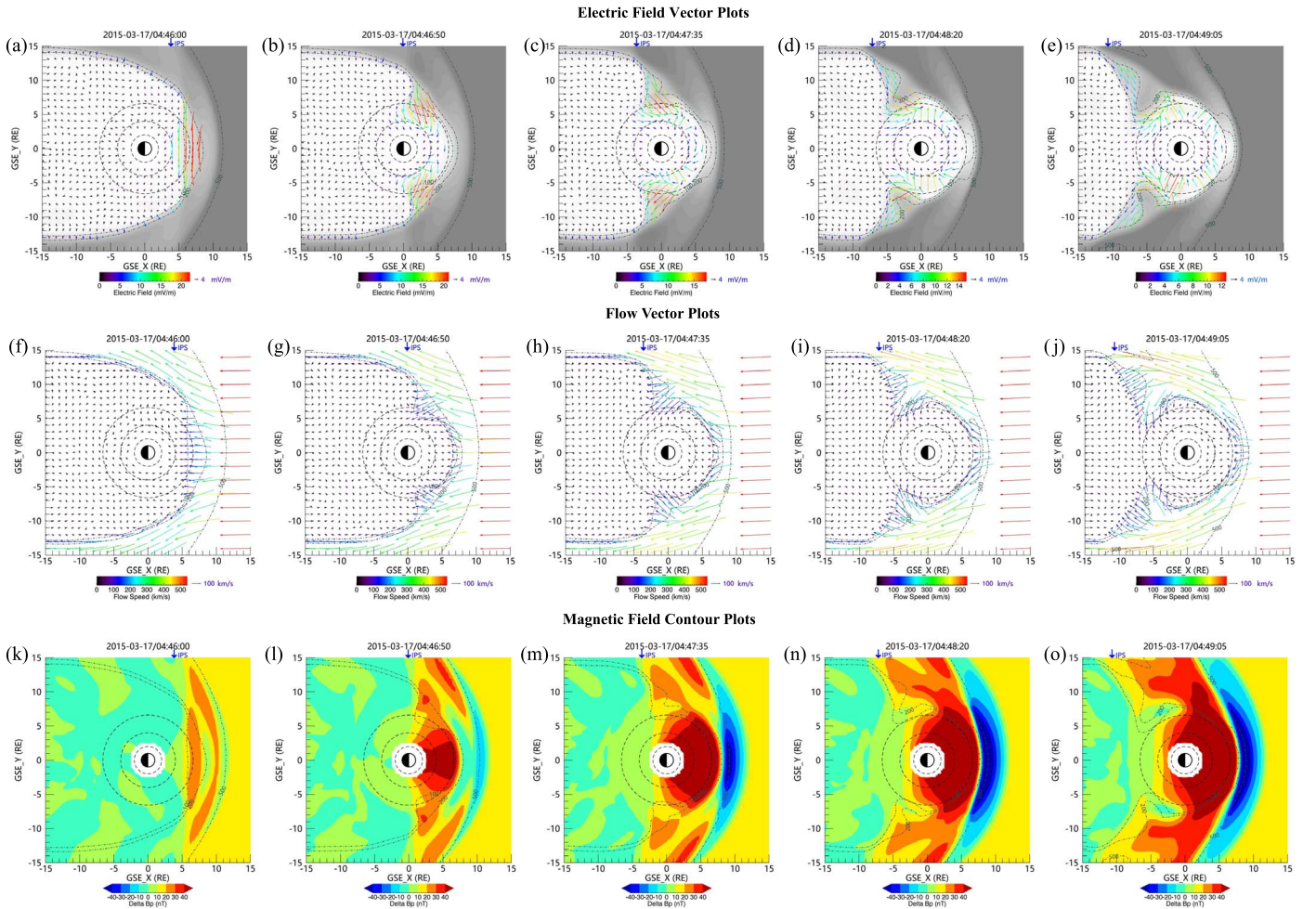


Figure 2. Evolution scenarios of electric field, flow, and magnetic field magnitude in global magnetosphere. (a)–(e) Electric field vector plots, (f)–(j) flow vector plots, and (k)–(o) magnetic field magnitude contour plots in GSE equatorial plane. Time sequence orders from left to right. Dashed–dotted lines represent the contour lines where flow speed equals 100, 200, or 500 km s^{-1} in each panel as labeled. Gray shade in (a)–(e) represents the region where flow speed is greater than 200 km s^{-1} . Density of the vectors are reduced outside the magnetosphere in the flow vector plots. The location of IPS is marked by blue arrows in each panel. Relevant animation of complete evolution scenarios of electric field, flow, and magnetic field magnitude (from left to right in animation) is also available with a duration of 24 s and a time resolution of 5 s.

(An animation of this figure is available.)

to the drift direction of radiation-belt electrons and thus is significant for radiation-belt dynamics. In Figures 2(a)–(c), the E_y impulse in the range of $L < 6.6$ is mainly westward due to the inward compressive motion of the magnetopause, according to the flow vector plot as shown in Figures 2(f)–(h). It is also worth noting that in the flank region there is downward electric field at the leading edge of the main E_a impulse as it propagates tailward as shown in Figure 2(b), which will be discussed in the following sections in further detail. In Figures 2(i)–(j), the compression-related inward plasma flows start to turn sunward (around regions of MLT ~ 21 and MLT ~ 3 and at $L \sim 5$) and then could eventually evolve into vortices both in dawnside and duskside, which correspond to westward E_a as shown in Figures 2(d)–(e).

For each location, the time series of E_y can be obtained from the simulation; three representative examples of the variation of E_y in time are shown in Figures 3(a)–(c) respectively, and correspond to a negative E_y impulse (dawnward, type I), a positive E_y impulse with leading negative E_y dip (dawnward-then-duskward, type II) and a positive E_y impulse (duskward, type III). Time series were obtained in a similar manner for all

locations on the equatorial plane, and were characterized according to the three types described in Figures 3(a)–(c). The distribution of these types in the equatorial plane is shown in Figure 3(d), with type I E_y impulses appearing mostly in the dayside, type III E_y impulses appearing in the midnight sector, and type II E_y impulses appearing in the postdusk and predawn sector. The directions of the electric field corresponding to the main peak of the impulses of all types are consistent with the description in the previous paragraph suggesting global compression. However, in the postdusk or predawn sectors the negative E_y dips are observed prior to the main E_y positive peak, which could be a clue indicating that the mechanism behind the electric field variation can be complicated rather than simply due to one mechanism, as discussed below.

4. Discussion

As mentioned in the introduction, two mechanisms need to be invoked to explain the different features of the IPS-induced electric field variation in the Earth’s magnetosphere: (1) the first mechanism involves the tailward propagation of fast-mode waves that are launched by the IPS’s impact on the dayside

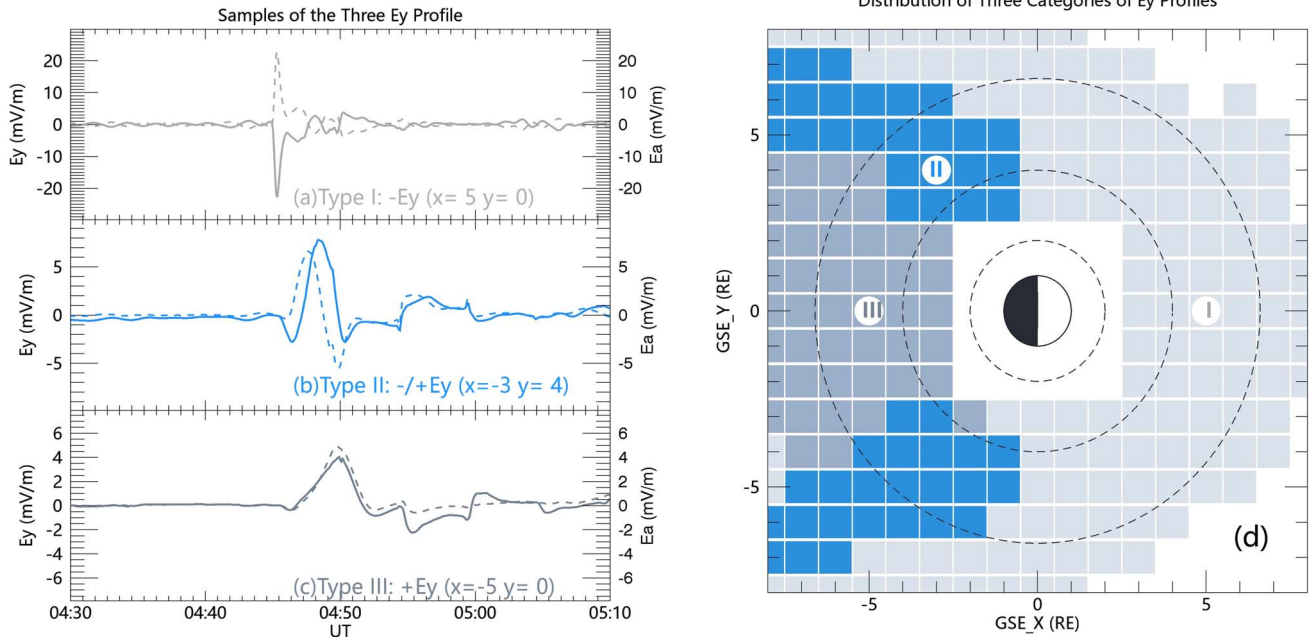


Figure 3. Three different types of E_y temporal profiles in the magnetosphere. (a)–(c) Examples of three different types of E_y profiles in simulation results, and (d) spatial distribution of the three different types in the equatorial plane. E_y profiles are plotted in solid lines with positive for duskward direction. E_a profiles are plotted in dashed lines with positive for westward direction for comparison.

magnetopause; and (2) the second mechanism involves the plasma flow related to the magnetopause motion caused by the passage of the IPS. In this paper, we focus on the rising phase of the first electric field impulse that is directly associated with the effect of the IPS. After the first impulse, the variations would eventually evolve into a vortex on the flank region as discussed by previous related numerical and observational studies (Kim et al. 2009; Shi et al. 2014), which is beyond the scope of this study.

On the dayside, as the IPS first contacts the dayside magnetopause (near the subsolar point), the compression on the magnetopause simultaneously launches fast-mode waves and earthward plasma flow, both of which correspond to dawnward electric field (negative E_y) variations. In the postdusk and predawn region, as the IPS passes through the flank regions, the tailward-propagating fast-mode wave generated on the dayside magnetopause propagates faster in the magnetosphere than the IPS in the magnetosheath, first resulting in a dawnward electric field (negative E_y) impulse. As the IPS subsequently impinges on the magnetopause, a compression-induced earthward flow is generated near the magnetopause, and a superposed sunward plasma flow starts to generate on the rear side of the earthward flow as shown in Figures 2(i)–(j), probably due to Kelvin–Helmholtz instability (Samsonov & Sibeck 2013; Shi et al. 2014; Sibeck 1990). The sunward-turning flow is responsible for the subsequent duskward electric field (positive E_y) impulse as shown in Figures 2(d)–(e). In the midnight sector, the fast-mode wave gradually decays as it propagates more tailward, which weakens the amplitude of the negative dip of the impulse, as shown by the comparison of type II and III in Figure 3. The impulse in the nightside magnetosphere is dominated by sunward-turning flow, which results in a pure duskward electric field (positive E_y) impulse. This sunward flow is induced by the passage of the IPS and eventually evolves into a large-scale vortex (Kim et al. 2009; Samsonov & Sibeck 2013; Shi et al.

2014; Sibeck 1990; also see the animation of Figure 2). This can also be confirmed by the simulated magnetic field depletion (Sun et al. 2015) near the inward flow at the magnetospheric flank as shown in Figure 2(o).

To summarize the scenario, the dawnward electric field variation (type I) on the dayside mainly corresponds to the combination of the propagation of the fast-mode wave and the flow induced by the compression of the dayside magnetopause; the dawnward-then-duskward electric field variation (type II) corresponds to the successive arrival of negative E_y dip induced by the dayside fast-mode wave and the positive E_y impulse induced by the compression-induced turning flow on the flank region; the duskward electric field variation on the nightside (type III) corresponds to the compression-related turning flow initiated on the flanks. It is suggested that the evolution of the impulse is a contribution of both the propagation of the fast-mode waves and the passage of the IPS.

The existence of the negative E_y dip of the type II impulse suggests that the formation of the impulse should be related to both mechanisms, which have different propagation speed leading to different profiles of the rising phase in different local time sectors. Thus we investigate the rise time of the impulse for further evidence, as shown in Figure 4. Two timescales are estimated for the propagation time from the subsolar point at $x = 10 R_E$ ($t = 0$) to a virtual spacecraft placed at $L = 5$ (left) and 6 (right) and for MLT = 3 to 21, based on each of the two mechanisms. The first timescale corresponds to the fast-mode wave travel time from the subsolar point to the virtual spacecraft, and is estimated as $t_1 = d_s/V_A$, where d_s is the distance between the subsolar point and the virtual spacecraft, and V_A is the average Alfvén speed along the path. In this study, V_A is set as 1032 km s^{-1} , which is the average value in the region of $3.5 < L < 7.5$ in the simulation. The second timescale corresponds to the propagation time of the magnetopause compression by the IPS, and is estimated as $t_2 = d_x/V_{\text{shock}}$, where d_x is the difference in the x direction between

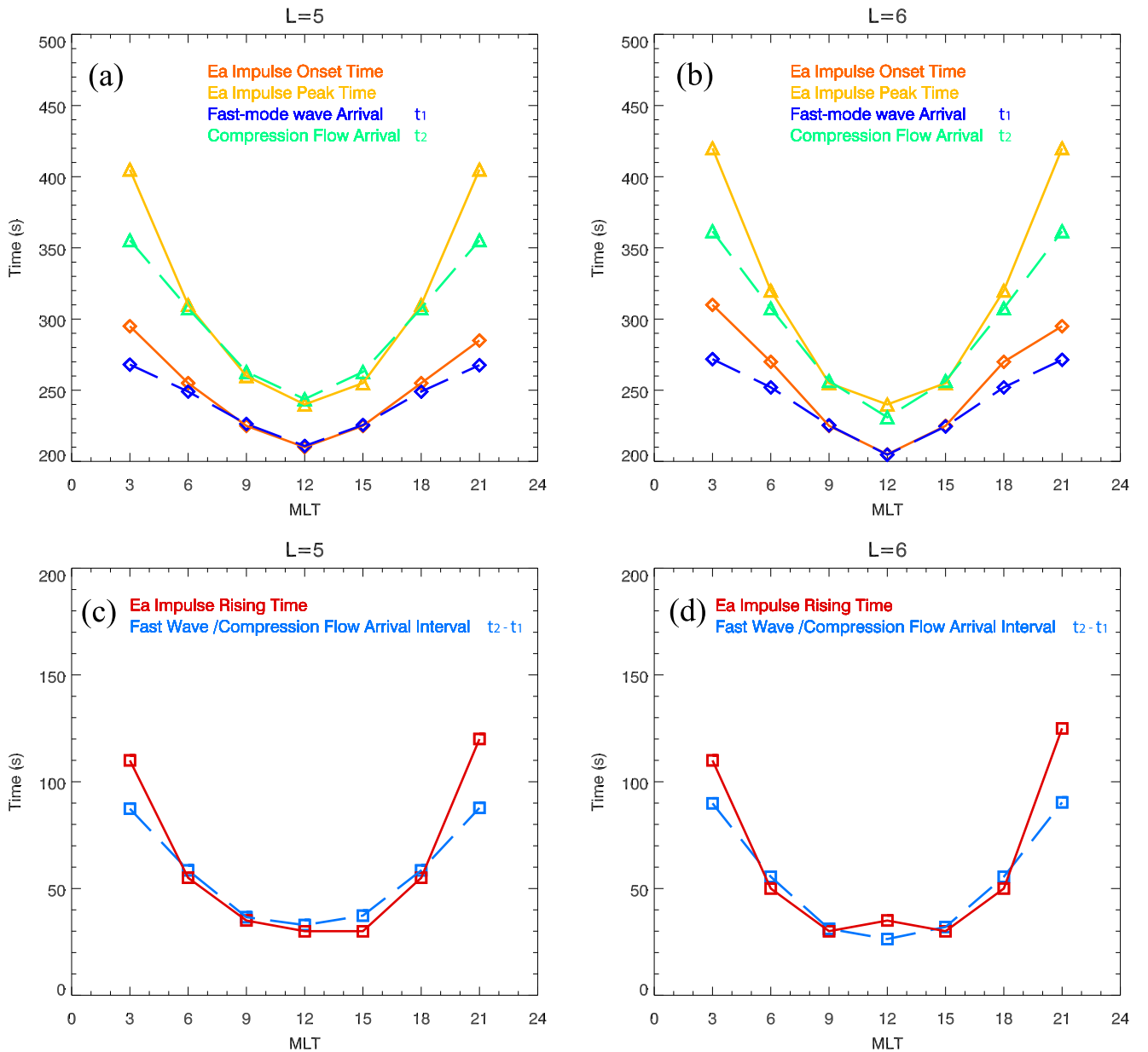


Figure 4. Comparison between simulated and theoretically estimated onset time, peak time, and rising time of electric field impulses. (a) and (b) Comparison between simulated onset time (red), peak time (orange) of electric field impulses, theoretically estimated fast-mode wave arrival time (blue), and compression-related flow arrival time (green) for $L = 5$ and $L = 6$ respectively. (c) and (d) Comparison between simulated (red) and theoretically estimated (blue) rising time for $L = 5$ and $L = 6$ respectively.

the subsolar point and the virtual spacecraft, and V_{shock} is the average propagation speed of the IPS, which is set as 537 km s^{-1} derived from the flow vector plots in Figures 2(f) – (j). The calculated t_1 and t_2 times are then plotted as dashed lines, in Figures 4(a) and (b) for $L = 5$ and $L = 6$ respectively. The timescales obtained from the simulation are plotted as solid lines for comparison, and are found to be consistent with the theoretical estimates based on the two proposed mechanisms. It is thus suggested that the onset of the electric field impulse is determined by the propagation of the fast-mode wave in the magnetosphere while the peak of the impulse is determined by the propagation of the compression on the magnetopause.

The rise time of the electric field impulse is also important, especially for the subsequent generation of ULF waves (Zhang et al. 2020) and the related radiation-belt electron acceleration (Li et al. 1993; Hudson et al. 2017). The rise times obtained

from the simulation are plotted as red solid lines in Figures 4(c) and (d) for $L = 5$ and $L = 6$ respectively. The theoretical estimates of the difference between t_1 and t_2 are plotted as blue dashed lines, demonstrating a good agreement between theory and simulation. It is shown that for the same L value, the rise time of the azimuthal electric field on the dayside is shorter than it is on the nightside, and as it closer to the midnight sector, the rise time becomes longer, which is consistent with the statistical results of our previous observational studies (Zhang et al. 2018, 2020).

The new scenario proposed in this paper can help better understand the prompt electron acceleration of radiation-belt electrons during IPS onsets. One can imagine that the electric field impulse travels azimuthally eastward in magnetosphere’s dusk sector, which is consistent with the electrons’ drifting direction. Thus, electrons that can stay in phase with the

electric field impulse are more likely to gain energy with the requirement that the drift velocity of the electrons be comparable to the azimuthal propagation speed of the electric field impulse. From Figure 4(a) for $L=5$, the peak of the impulse travels azimuthally from 12 to 21 MLT within 200 s, corresponding to a velocity of about 375 km s^{-1} , consistent with the drift velocity of electrons with energy in the range of $2.5 \sim 3.0 \text{ MeV}$. It has been shown in previous observation and simulation studies of the same event that electrons in this energy range are more efficiently accelerated than at lower energies (Hudson et al. 2017; Kanekal et al. 2016).

From our theoretical calculation, there are two parameters controlling the temporal profile of an impulse: these are the local Alfvén speed, V_A , and the propagation speed of the IPS, V_{shock} , both of which can be easily obtained based on measurements in magnetosphere or solar wind. With these two parameters, our scenario is able to predict the azimuthally propagating speed of the impulse, which is important for prompt electron injection, and the rise time of the impulse, which is important for the generation of subsequent ULF waves and of electron acceleration through drift resonance and sheds new light on the understanding of the interaction of the IPS with the inner magnetosphere.

During most IPS events, V_A is reported to be about $600\text{--}1000 \text{ km s}^{-1}$ (Cattell et al. 2017; Takahashi et al. 2017; Zong et al. 2009) in the inner magnetosphere, which is larger than V_{shock} varying from 300 to 600 km s^{-1} . However, for extreme events like the 1991 March 24 event, V_{shock} could possibly reach 2000 km s^{-1} , which is much larger than V_A , which might lead to different characteristics of the responses in the magnetosphere because shocks could be formed in the magnetosphere, and thus requires more investigation in future study.

5. Conclusion

Combining the Van Allen Probes observation with the SWMF model simulation, we investigate the propagation of the electric field impulse induced by IPS's compression event of 2015 March 17. Both in the observation and in the simulation, a dip-like impulse profile in the E_y data (dawnward then duskward) is identified. Based on the investigation on this type of electric field impulse, we propose a new scenario that the IPS-induced electric field impulse is a consequence of the superposed effect successively of the fast-mode wave generated from the dayside, magnetopause near-subsolar point and the compression-induced flow related to passage of the IPS at the magnetopause flank region. This new scenario is more capable of explaining the previous observations and simulations of the IPS-induced electric field impulse. Furthermore, as an aspect of the temporal characteristics, we found that the onset and peak of the electric field impulse respectively correspond to the arrival of the fast-mode wave and the IPS, and this feature could greatly affect the energy of the injected and accelerated electrons in the radiation belt.

This work was supported by the National Natural Science Foundation of China grants 41821003, 41974194, and 41974192. This work was carried out using the SWMF and BATS-R-US tools developed at the University of Michigan's Center for Space Environment Modeling (CSEM). Simulations were performed over the Tianhe-2 National Supercomputer Center at Guangzhou, China. We thank the EFW and EMFISIS

teams of the Van Allen Probes mission, 3DP and MFI teams of Wind mission, and OMNI database for making data available.

ORCID iDs

Dianjun Zhang  <https://orcid.org/0000-0002-7312-0551>
 Wenlong Liu  <https://orcid.org/0000-0001-7991-5067>
 Yiqun Yu  <https://orcid.org/0000-0002-1013-6505>
 Xinlin Li  <https://orcid.org/0000-0002-1683-3192>
 Theodore E Sarris  <https://orcid.org/0000-0002-0336-2678>
 Jinbin Cao  <https://orcid.org/0000-0002-5637-2976>

References

- Araki, T. 1997, *JGRA*, **102**, 14075
 Baumjohann, W., Junginger, H., Haerendel, G., & Bauer, O. H. 1984, *JGR*, **89**, 2765
 Blake, J. B., Kolasinski, W. A., Fillius, R. W., & Mullen, E. G. 1992, *GeoRL*, **19**, 821
 Cattell, C., Breneman, A., Colpitts, C., et al. 2017, *GeoRL*, **44**, 8712
 De Michelis, P., Pignalberi, A., Consolini, G., et al. 2020, *JGRA*, **125**, e27934
 De Zeeuw, D. L., Sazykin, S., Wolf, R. A., et al. 2004, *JGRA*, **109**, A12219
 Dmitriev, A. V., Suvorova, A. V., Klimenko, M. V., et al. 2017, *JGRA*, **122**, 2398
 Eriksson, P. T., Blomberg, L. G., Schaefer, S., & Glassmeier, K. H. 2006, *AnGeo*, **24**, 3161
 Foster, J. C., Wygant, J. R., Hudson, M. K., et al. 2015, *JGRA*, **120**, 1661
 Fu, H., Cao, J., Mozer, F., Lu, H., & Yang, B. 2012, *JGRA*, **117**, A01203
 Fu, H., Cao, J., Yang, B., & Lu, H. 2011, *JGRA*, **116**, A10210
 Goldstein, J., Angelopoulos, V., De Pascuale, S., et al. 2017, *JGRA*, **122**, 368
 Hao, Y. X., Zong, Q. G., Wang, Y. F., et al. 2014, *JGRA*, **119**, 8262
 Hao, Y. X., Zong, Q. G., Zhou, X. Z., et al. 2019, *JGRA*, **124**, 1525
 Hudson, M., Jaynes, A., Kress, B., et al. 2017, *JGRA*, **122**, 10036
 Hudson, M. K., Denton, R. E., Lessard, M. R., Miftakhova, E. G., & Anderson, R. R. 2004, *AnGeo*, **22**, 289
 Hudson, M. K., Paral, J., Kress, B. T., et al. 2015, *JGRA*, **120**, 1168
 Jaynes, A. N., Ali, A. F., Elkington, S. R., et al. 2018, *GeoRL*, **45**, 10874
 Kanekal, S. G., Baker, D. N., Fennell, J. F., et al. 2016, *JGRA*, **121**, 7622
 Kim, K. H., Lee, D. H., Shiokawa, K., et al. 2012, *JGRA*, **117**, A10209
 Kim, K. H., Park, K. S., Ogino, T., et al. 2009, *JGRA*, **114**, A08212
 Kletzing, M. A., Kurth, W. S., Acuna, M., et al. 2013, *SSRv*, **179**, 127
 Korotova, G., Sibeck, D., Thaller, S., et al. 2018, *AnGeo*, **36**, 1319
 Kress, B. T., Hudson, M. K., Looper, M. D., et al. 2007, *JGRA*, **112**, A09215
 Kubyskhina, M., Sergeev, V. A., Tsyganenko, N. A., & Zheng, Y. 2019, *SpWea*, **17**, 672
 Lepping, R. P., Acuna, M. H., Burlaga, L. F., et al. 1995, *SSRv*, **71**, 207
 Lepping, R. P., Jones, J. A., & Burlaga, L. F. 1990, *JGR*, **95**, 11957
 Li, L. Y., Yu, J., Cao, J. B., & Yuan, Z. G. 2016, *PhPl*, **23**, 062116
 Li, X., Roth, I., Temerin, M., et al. 1993, *GeoRL*, **20**, 2423
 Liu, W., Cao, J., Li, X., et al. 2013, *JGRA*, **118**, 4298
 Liu, W., Sarris, T. E., Li, X., et al. 2009, *JGRA*, **114**, A12206
 Liu, W., Sarris, T. E., Li, X., et al. 2010, *JGRA*, **115**, A12201
 Liu, Y., Zong, Q. G., Zhou, X. Z., Hao, Y. X., & Liu, Z. Y. 2019, *JGRA*, **124**, 6759
 Lyons, L. R., Gallardo-Lacourt, B., Zou, S., et al. 2016, *JGRA*, **121**, 10880
 Marsal, S., Torta, J. M., Segarra, A., & Araki, T. 2017, *JGRA*, **122**, 194
 Mauk, B. H., Fox, N. J., Kanekal, S. G., et al. 2013, *SSRv*, **179**, 3
 Ozeke, L. G., Mann, I. R., Claudepierre, S. G., et al. 2019, *JGRA*, **124**, 1143
 Papadimitriou, C., Balasis, G., Boutsis, A. Z., et al. 2020, *Entp*, **22**, 574
 Patel, M., Li, Z., Hudson, M., Claudepierre, S., & Wygant, J. 2019, *GeoRL*, **46**, 7222
 Powell, K. G., Roe, P. L., Linde, T. J., Gombosi, T. I., & De Zeeuw, D. L. 1999, *JCoPh*, **154**, 284
 Prikryl, P., Ghoddousi-Fard, R., Weygand, J. M., et al. 2016, *JGRA*, **121**, 10448
 Rastätter, L., Kuznetsova, M. M., Glocer, A., et al. 2013, *SpWea*, **11**, 187
 Ridley, A. J., Gombosi, T. I., & DeZeeuw, D. L. 2004, *AnGeo*, **22**, 567
 Samsonov, A. A., & Sibeck, D. G. 2013, *JGRA*, **118**, 3055
 Samsonov, A. A., Sibeck, D. G., & Yu, Y. 2010, *JGRA*, **115**, A05207
 Schiller, Q., Kanekal, S. G., Jian, L. K., et al. 2016, *GeoRL*, **43**, 12317
 Shi, Q. Q., Hartinger, M., Angelopoulos, V., et al. 2014, *JGRA*, **119**, 4274
 Shinbori, A., Ono, T., Iizima, M., & Kumamoto, A. 2004, *EP&S*, **56**, 269
 Sibeck, D. G. 1990, *JGR*, **95**, 3755
 Sun, T. R., Wang, C., Zhang, J. J., et al. 2015, *JGRA*, **120**, 157

- Takahashi, N., Kasaba, Y., Nishimura, Y., et al. 2017, *JGRA*, **122**, 8446
- Toffoletto, F., Sazykin, S., Spiro, R., & Wolf, R. 2003, *SSRv*, **107**, 175
- Tóth, G., Sokolov, I. V., Gombosi, T. I., et al. 2005, *JGRA*, **110**, A12226
- Wang, C., Liu, J. B., Li, H., et al. 2009, *JGRA*, **114**, A05211
- Wang, H., Lühr, H., Ridley, A., Ritter, P., & Yu, Y. 2008, *AnGeo*, **26**, 555
- Wei, D., Yu, Y., & He, F. 2019a, *GeoRL*, **46**, 7079
- Wei, D., Yu, Y., Ridley, A. J., Cao, J., & Dunlop, M. W. 2019b, *AdSpR*, **63**, 3522
- Welling, D. T., & Ridley, A. J. 2010, *SpWea*, **8**, 03002
- Wilken, B., Goertz, C. K., Baker, D. N., Higbie, P. R., & Fritz, T. A. 1982, *JGRA*, **87**, 5901
- Wygant, J., Bonnell, J., Goetz, K., et al. 2013, *SSRv*, **179**, 183
- Yu, Y., & Ridley, A. J. 2008, *SpWea*, **6**, 05002
- Yu, Y., & Ridley, A. J. 2009, *AnGeo*, **27**, 4391
- Yu, Y., & Ridley, A. J. 2011, *JGRA*, **116**, A04210
- Yue, X., Wan, W., Liu, L., et al. 2016, *JGRA*, **121**, 12202
- Zakharenkova, I., Astafyeva, E., & Cherniak, I. 2016, *JGRA*, **121**, 12138
- Zhang, D., Liu, W., Li, X., et al. 2018, *GeoRL*, **45**, 7287
- Zhang, D., Liu, W., Li, X., et al. 2020, *GeoRL*, **47**, e90027
- Zhang, S.-R., Erickson, P. J., Zhang, Y., et al. 2017, *JGRA*, **122**, 1314
- Zhang, X. Y., Zong, Q. G., Wang, Y. F., et al. 2010, *JGRA*, **115**, A10221
- Zhang, Y., Paxton, L. J., Immel, T. J., Frey, H. U., & Mende, S. B. 2003, *JGRA*, **108**, 8001
- Zhou, X., & Tsurutani, B. T. 1999, *GeoRL*, **26**, 1097
- Zong, Q. G., Zhou, X. Z., Wang, Y. F., et al. 2009, *JGRA*, **114**, A10204